

Magnetic helicity effects in astrophysical and laboratory dynamos

A Brandenburg^{1,3} and P J Käpylä^{1,2}

¹ NORDITA, AlbaNova University Center, SE-10691 Stockholm, Sweden

² Observatory, University of Helsinki, P O Box 14, FI-00014, Finland

E-mail: brandenb@nordita.dk

New Journal of Physics **9** (2007) 305

Received 3 March 2007

Published 31 August 2007

Online at <http://www.njp.org/>

doi:10.1088/1367-2630/9/8/305

Abstract. Magnetic helicity effects are discussed in laboratory and astrophysical settings. Firstly, dynamo action in Taylor–Green flows is discussed for different boundary conditions. However, because of the lack of scale separation with respect to the container, no large-scale field is being produced and there is no resistively slow saturation phase as otherwise expected. Secondly, the build-up of a large-scale field is demonstrated in a simulation where a localized magnetic eddy produces field on a larger scale if the eddy possesses a swirl. Such a set-up might be realizable experimentally through coils. Finally, new emerging issues regarding the connection between magnetic helicity and the solar dynamo are discussed. It is demonstrated that dynamos with a nonlocal (Babcock–Leighton type) α effect can also be catastrophically quenched, unless there are magnetic helicity fluxes.

³ Author to whom any correspondence should be addressed.

Contents

1. Introduction	2
2. Governing equations	3
3. Lorenz versus Weyl gauge	4
4. TG flow dynamos	5
5. Inverse transfer from a localized source	10
6. Connection with the solar dynamo problem	11
6.1. Catastrophic η_t quenching?	12
6.2. Catastrophic α quenching and nonlocality	13
6.3. Location of the dynamo	16
6.4. Predictability in distributed dynamos	18
7. Conclusions	20
Acknowledgments	20
Appendix A. Magnetic versus kinetic helicity conservation	20
Appendix B. The forcing function	22
Appendix C. One-mode truncation of the Blackman–Field model	23
References	23

1. Introduction

Many astrophysical dynamos are driven by helical flows via an α effect. Helical flows are also employed in all laboratory realizations of liquid metal dynamos. One of the remarkable properties of helical dynamos is that they produce large-scale fields that are helical. Since net helicity is conserved, this can only happen if there is a production of an equal amount of small-scale fields with opposite helicity. This has been demonstrated through various numerical studies (Brandenburg 2001, Mininni *et al* 2005a).

An obvious question is whether these properties can also be seen in experimental realization of fluid dynamos. The preliminary answer to this is no, because there is no scale separation. We will return to this in more detail and present new calculations of Taylor–Green (TG) flows that model the flow in the French VKS2 experiment (Monchaux *et al* 2007). To address the issue of the lack of scale separation we also study a model designed to show the development of large-scale magnetic fields that are driven from a small localized source. Finally, we discuss some new issues regarding the solar dynamo.

We assume some level of familiarity with the concept of magnetic helicity conservation and the resistively limited saturation phenomenon found in the nonlinear evolution of large-scale dynamos. In this connection, we highlight the usage of the word ‘catastrophic’, which is meant to indicate that the result depends on the value of the magnetic Reynolds number. This applies in particular to the α effect which is now known to be catastrophically quenched when there is no flux of magnetic helicity. A recent review on the development of the last five years can be found in Brandenburg and Subramanian (2005a).

Throughout this paper we present original results that have not yet been presented earlier. Many of the cases considered are motivated by the recent developments in laboratory dynamos and solar dynamo modelling. Many of the simulations have been carried out at relatively low

resolution. The present results are therefore tentative and need to be followed up using higher resolution simulations. However, the results presented here do reflect the current state of affairs in this field, which is indeed one of the objectives of this paper.

2. Governing equations

We consider here the isothermal and weakly compressible case, which means that the pressure gradient term can be written as a gradient of the pseudo enthalpy⁴, $h = c_s^2 \ln \rho$, where $c_s = \text{const.}$ is the isothermal speed of sound and ρ is the density. The induction equation can then be written in an analogous form in terms of the magnetic vector potential by using the pseudo Lorenz gauge with a freely specified speed c_ϕ , which is for practical reasons less than the speed of light, and may well be equal to the speed of sound c_s . The set of equations is thus

$$\frac{\partial \mathbf{A}}{\partial t} = -\nabla \phi + \mathcal{E}_{\text{ext}} - \eta \mathbf{J} + \mathbf{u} \times \mathbf{B}, \quad \frac{\partial \phi}{\partial t} = -c_\phi^2 \nabla \cdot \mathbf{A}, \quad (1)$$

$$\frac{D\mathbf{U}}{Dt} = -\nabla h + \mathcal{F}_{\text{ext}} - \nu \mathbf{Q} + \mathbf{J} \times \mathbf{B}/\rho, \quad \frac{Dh}{Dt} = -c_s^2 \nabla \cdot \mathbf{U}, \quad (2)$$

where \mathbf{U} is the velocity, $\mathbf{B} = \nabla \times \mathbf{A}$ is the magnetic field, expressed in terms of the magnetic vector potential \mathbf{A} , $\mathbf{J} = \nabla \times \nabla \times \mathbf{A}$ is the current density, $\mathbf{Q} = \nabla \times \nabla \times \mathbf{U}$ is the double curl of the velocity, $D/Dt = \partial/\partial t + \mathbf{U} \cdot \nabla$ is the advective derivative, and \mathcal{E}_{ext} and \mathcal{F}_{ext} are external forcing functions, to be specified later. The current density is measured in units where the vacuum permeability is unity. The main analogy we want to stress here is that between the electric potential ϕ in the uncurled induction equation and the pseudo enthalpy h in the momentum equation. We should point out that, in order to not disturb the analogy between the two equations, we have ignored a correction term in equation (1) where \mathbf{Q} has to be replaced by

$$\mathbf{Q} \rightarrow \mathbf{Q} + \nabla \nabla \cdot \mathbf{U} + \mathbf{S} \cdot \nabla \ln(\rho \nu), \quad (3)$$

where $\mathbf{S}_{ij} = \frac{1}{2}(U_{i,j} + U_{j,i}) - \frac{1}{3}\delta_{ij} \nabla \cdot \mathbf{U}$ is the traceless rate of strain tensor. For incompressible flows these correction terms vanish, and they are small for weakly compressible (small Mach number) flows considered here. Nevertheless, in the numerical computations these extra terms in equation (3) are always included.

If we think of the velocity field being primarily just the vector potential for the vorticity (see appendix A), then we can regard the continuity equation, $Dh/Dt = -c_s^2 \nabla \cdot \mathbf{U}$, as the gauge condition for the velocity in the Lorenz-like gauge. In this sense we can interpret the Lorenz gauge condition for \mathbf{A} as a continuity equation for ϕ . Note, however, that \mathbf{A} is not a physically measurable quantity.

⁴ For a polytropic gas the enthalpy can be written as $h = (\gamma - 1)^{-1} c_{s0}^2 (\rho/\rho_0)^{\gamma-1}$, which reduces to $c_{s0}^2 \ln(\rho/\rho_0) + \text{const}$ in the limit of $\gamma \rightarrow 1$. In the following we ignore the above constant in our definition of the enthalpy and refer to it therefore as the pseudo enthalpy.

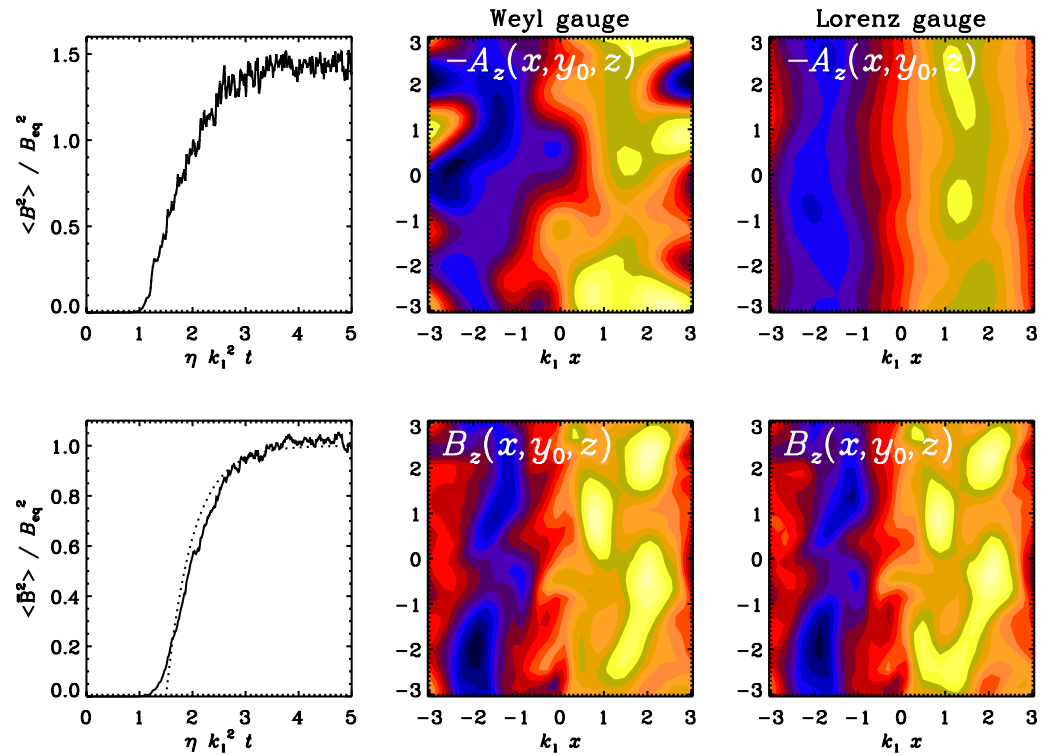


Figure 1. Comparison of runs in Weyl and Lorenz gauges. In this simulation a large-scale magnetic field develops owing to the helicity of the velocity forcing function. While the magnetic field is the same in both gauges (second and third column in the second row) and vector potential is different (second and third column in the first row). These slices are taken after three magnetic diffusion times. For comparison, the evolution of magnetic energy in the total field (upper left panel) and in the mean field (lower left panel) are shown, where time is given in diffusion times.

3. Lorenz versus Weyl gauge

Magnetic and electric fields are invariant under the gauge transformation

$$A' = A + \nabla \Lambda, \quad (4)$$

$$\phi' = \phi - \frac{\partial \Lambda}{\partial t}. \quad (5)$$

For numerical purposes it is often convenient to choose the gauge $\Lambda = \int \phi dt$, which implies that $\phi' = 0$. Thus, instead of equation (1) one solves the equation $\partial A' / \partial t = -E$. The latter is usually referred to as the Weyl gauge.

In this section, we compare the two gauges. Obviously the magnetic field is the same in both cases, but the magnetic vector potential is not. In figure 1, we compare the results obtained with the two techniques in the case of a dynamo driven by fully helical turbulence. The detailed forcing function used here is given in appendix B. We choose 32^3 mesh points, a forcing wavenumber

of $k_f = 3k_1$, where k_1 is the smallest wavenumber in the box, and a forcing amplitude of 0.07, which results in an rms velocity of about 0.2. Viscosity and magnetic diffusivity are chosen to be 5×10^{-3} , so the magnetic Reynolds number is $R_m = u_{\text{rms}}/(\eta k_f) = 13$. For details about these and similar runs at larger magnetic Reynolds number, see Brandenburg (2001), which is also where the resistively limited saturation phase with

$$\langle \bar{B}^2 \rangle \propto 1 - e^{-2\eta k_1^2(t-t_{\text{sat}})} \quad (6)$$

was proposed. Here, t_{sat} is the time where the small-scale magnetic field saturates. The dotted line in the lower left panel shows this behaviour.

For the present studies we used just 32^3 meshpoints, which can easily run on one processor using the PENCIL CODE⁵ which is a nonconservative, high-order, finite-difference code (sixth-order in space and third-order in time) for solving the compressible hydrodynamic equations. The particular run presented in this section is actually one of the sample runs (helical-MHDturb) that come with the code. Here and in all other cases presented in this paper we use $c_s = c_\phi = 1$.

Obviously, the resistive saturation phase becomes more prominent at larger Reynolds numbers. However, the point of this simulation was to illustrate the differences between Lorenz and Weyl gauges. Qualitatively, it appears that the magnetic vector potential in the Lorenz gauge is smoother than that in the Weyl gauge. In general, the divergence of the magnetic vector potential is small, so for all practical purposes the Lorenz gauge is close to the Coulomb gauge. One may hope that in the presence of open boundary conditions, where a gauge-invariant magnetic helicity is harder to define, the Lorenz-gauged magnetic vector potential may provide some meaningful guidance regarding the escape of magnetic helicity density and the associated magnetic helicity fluxes (cf Subramanian and Brandenburg 2006).

4. TG flow dynamos

The TG flow is often studied in connection with the von Kármán Sodium (VKS) dynamo experiment in Cadarache in France (Monchaux *et al* 2007). The TG flow is given by $\mathbf{U} = \mathcal{F}_{\text{ext}}/(vk_f^2)$, where $k_f = \sqrt{3}k_0$ and

$$\mathcal{F}_{\text{ext}} = 2f_0 \begin{pmatrix} + \sin k_0 x \cos k_0 y \cos k_0 z \\ - \cos k_0 x \sin k_0 y \cos k_0 z \\ 0 \end{pmatrix}, \quad -\frac{\pi}{k_0} < x, y, z < \frac{\pi}{k_0}. \quad (7)$$

The forcing function is normalized such that $\langle \mathcal{F}_{\text{ext}}^2 \rangle^{1/2} = f_0$. There is a vast literature on this flow. Due to a large number of symmetries allowing computational simplifications, large Reynolds numbers can be achieved. This flow has therefore been used to study singularities and turbulence (Brachet 1991, Nakano 1985). In more recent years dynamo action for this flow has been studied (Nore *et al* 1997), especially at low magnetic Prandtl numbers (Mininni *et al* 2005b, Ponty *et al* 2004, 2005).

In the following we use $f_0 = 0.006$, $\nu = 0.02$, so that $u_{\text{rms}} = 0.1$. We adopt units of length where $k_0 = 1$. In agreement with common practice, in this section we use Reynolds numbers based on the scale $1/k_0$ rather than $1/k_f$, i.e. $\text{Re} = u_{\text{rms}}/(\nu k_1)$ and $R_m = u_{\text{rms}}/(\eta k_1)$.

⁵ <http://www.nordita.dk/software/pencil-code>.

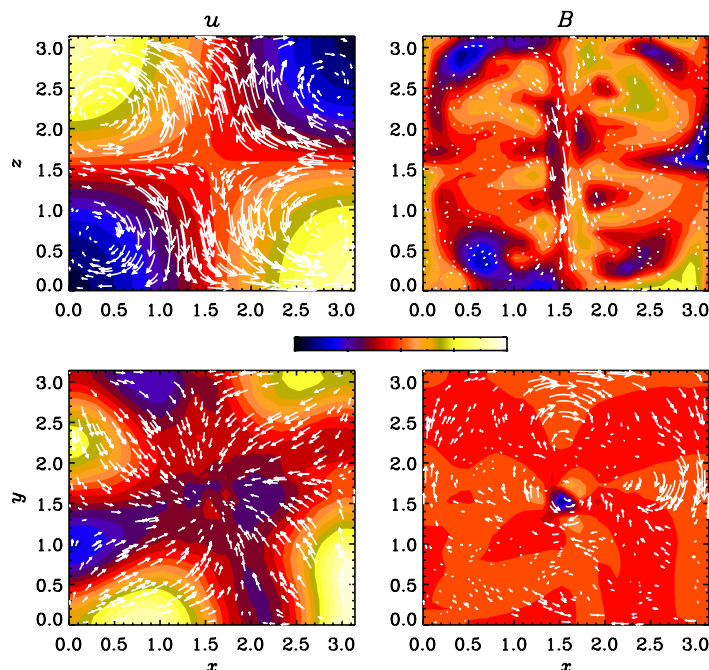


Figure 2. Cross-section through the middle of the domain ($y = \pi/2$ in the upper row and $z = \pi/2$ in the lower row) of velocity (left-hand column) and magnetic field (right-hand column). Velocity and magnetic fields are represented by vectors in the plane and colors (grey scales) indicate the normal components. The colored (grey scale) bar indicates the contour range symmetrically about zero within the maximum values of either sign. The light red color (intermediate grey) corresponds to zero. All boundaries are assumed to be *perfectly conducting*. $Re = 5$ and $R_m = 1000$.

No magnetic forcing is applied, i.e. $\mathcal{E}_{\text{ext}} = 0$. The VKS flow corresponds to one-eighth of the full domain, i.e. $0 < x, y, z < \pi$. Since dynamo action in the TG flow is normally studied in triply periodic domains we show in figure 2 numerically obtained results for a domain bounded by perfect conductors on all sides. In figure 3 we give the corresponding result for a domain where we adopt a ‘vertical field’ boundary condition on $z = 0$ and $z = \pi$. The latter is supposed to simulate the experimental situation of soft iron boundaries with a large permeability (E Dormy private communication, Fauve and Pétrélis (2003), Morin (2005); see also Kenjerescaron and Hanjalicacute (2007)). Finally, in figure 4 we show the result for a triply periodic domain. The resulting saturation field strengths for the three cases are summarized in table 1.

Evidently, the dynamo operation is quite sensitive to the boundary conditions in that the critical value of R_m is about five times larger when all domain boundaries are perfectly conducting. In this light it is not too surprising that no dynamo was found before using the soft iron lids at the two ends of the VKS experiment (Monchaux *et al* 2007). Indeed, the model with the vertical field condition has the lowest critical magnetic Reynolds number of all three cases considered. The field shows a narrow vertical flux tube in the middle of the domain. Obviously, given that our fluid Reynolds number is small, the velocity field is laminar. Larger Reynolds numbers could be achieved with more meshpoints.

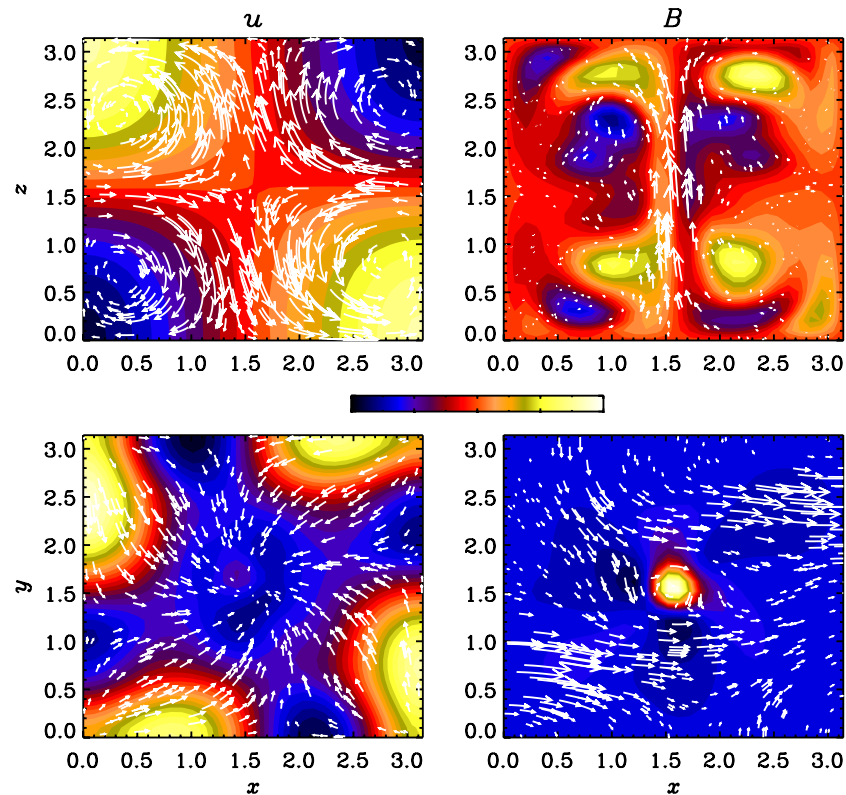


Figure 3. Same as figure 3, but with *vertical field* boundary conditions at $z = 0$ and $z = \pi$. $Re = 5$ and $R_m = 200$.

In figure 5 we show that the root mean square magnetic field strength saturates after about one magnetic diffusion time. Nevertheless, there is *no* prolonged saturation phase as it was seen in figure 1, or in other forced turbulence simulations where the forcing wavenumber k_f/k_1 is large. In figure 5 we also show the electric potential difference over a distance of 4 meshpoints. It turns out that the electric potential difference shows strong bursts during times when the field is strong. At late times the potential difference oscillates with a frequency of about 0.14, which is about seven times smaller than the basic frequency, $c_\phi k_1$.

The nature of the oscillations in figure 5 remains unclear. Similar oscillations have been seen in solutions of mean-field dynamo equations derived under the τ approximation where the explicit time derivative of the electromotive force is retained (Blackman and Field 2002). Such oscillations have also been seen in direct simulations of passive scalar turbulence, when the forcing scale is close to the scale of the domain (Brandenburg *et al* 2004). This is actually the case here, because $k_f/k_1 = \sqrt{3}$ is close to unity. However, there appear to be two problems with this interpretation, which are illustrated using a numerical solution of an appropriately adjusted version of the Blackman–Field model; see figure 6. This model is solved here in the one-mode truncation; see appendix C. Firstly, the frequency of the oscillations is in the model $\omega_{\text{osc}} = u_{\text{rms}} k_f \sqrt{3}$, but this is about 20 times higher than what is actually seen. Secondly, the slow saturation phase, as described by equation (6), should still be seen in the saturation of the mean field. For these reasons we can conclude that the behaviour seen in TG flow dynamos is not described by standard mean field models. It should also be noted that any mean field in these dynamos cannot be seen as spatial averages.

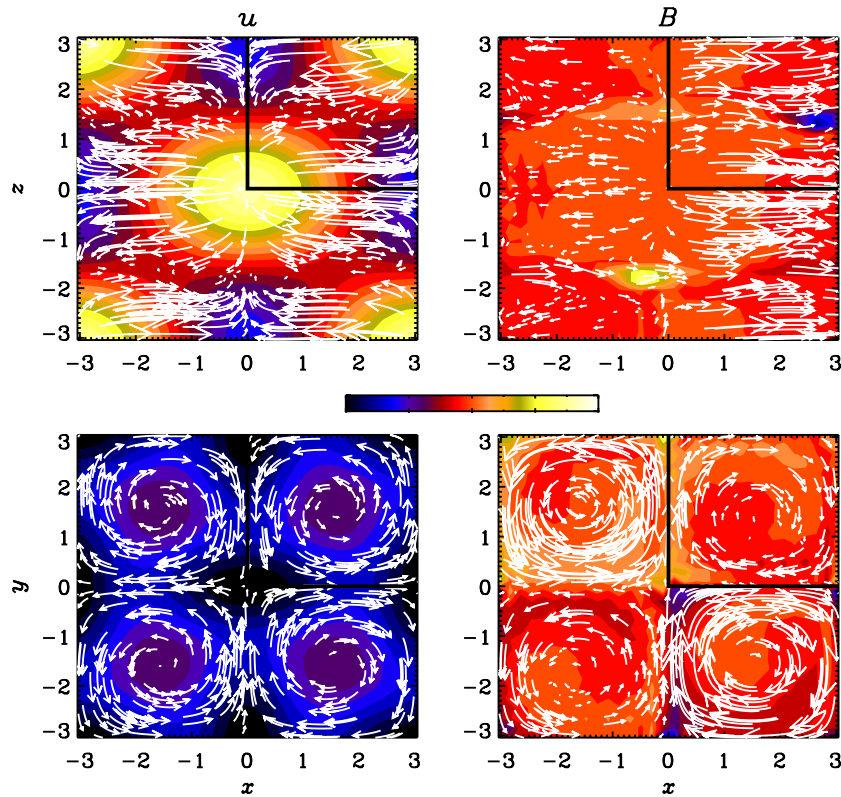


Figure 4. Same as figure 3, but for triply periodic boundary conditions in the larger domain, $-\pi < x, y, z < \pi$. The box in the first quadrant marks the location of the computational domains used for the results shown in figures 2 and 3. Note that the magnetic field is concentrated preferentially along the cell boundaries. $Re = 5$ and $R_m = 200$.

Table 1. Saturation values of $B_{\text{rms}} = \langle \mathbf{B}^2 \rangle^{1/2}$ for TG flow dynamo in triply-periodic domains of volume $(2\pi)^3$ (second column) compared with those in one-eighth of the volume (π^3), where the boundaries in the x - and y -directions are perfectly conducting, and those in the z -direction either using a vertical field boundary condition (third column) or also perfectly conducting (last column).

R_m	Periodic	Vertical field	Perfect conductivity
200	0	0.027	0
500	0.053	0.069	0
1000			0.041
2000			0.054

Temporal averages may be a useful way of analysing the evolution of mean fields in TG flow dynamo. It turns out that after saturation ($\eta k_f^2 t > 3$) the time averaged field contains about 88% of the total magnetic energy. At earlier times the oscillations are well reproduced by time averages over short enough time spans ($\eta k_f^2 \Delta t = 0.04$). No evidence for a slow resistively limited

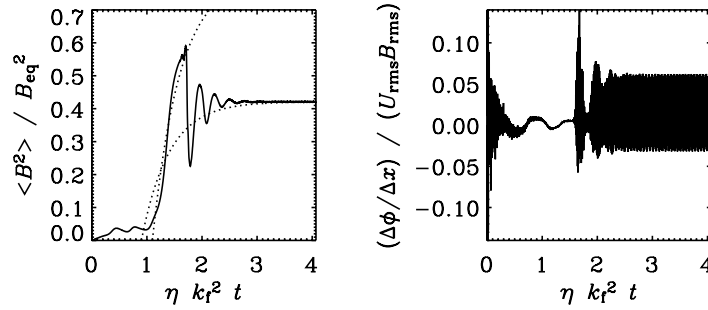


Figure 5. Saturation behaviour of a run with a vertical field boundary condition similar to that shown in figure 3 with $Re = 5$ and $R_m = 500$. The dotted lines represent failed attempts to match the saturation behaviour to the functional form of equation (6), so the saturation is not resistively limited in this case. Note the bursty oscillations in the electric potential difference during early times when the field becomes strong.

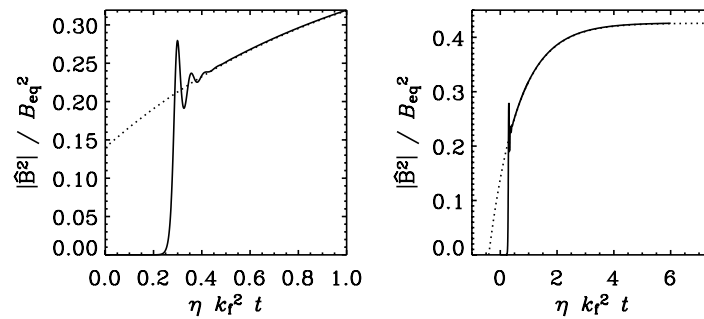


Figure 6. Solution of the one-mode truncation of the Blackman-Field model with $R_m = 500$ and $St = 20$. The left-hand panel more clearly shows the oscillations around the time $\eta k_f^2 t = 0.35$, while the right-hand panel shows the full saturation phase, which is matched perfectly by equation (6) as shown by the dotted line.

saturation phase is seen even for intermediate time averages. Again, this supports the idea that the magnetic fields seen in TG flow dynamos cannot be described by the existing mean field approach.

In hindsight the absence of a slow resistively limited saturation phase is not too surprising because the wavenumber of the forcing function, $k_f = \sqrt{3}k_0$, is close to the box wavenumber, so there is no scale separation. This means that any large-scale field, if it exists, could only be generated at almost the same scale. More importantly, because on short time scales no magnetic helicity can be generated, the positive magnetic helicity in the forcing must be balanced by the negative magnetic helicity at the same scale, leading essentially to a cancellation of the magnetic field.

In order for there to be a large-scale field, it is important to allow for a domain size that is sufficiently large to accommodate a field whose scale is at least a few times bigger than the eddy scale. In figure 7 we show the growth of the rms field strength of mean fields defined by averaging over different horizontal planes. Most interesting is the xy plane, and the corresponding averages

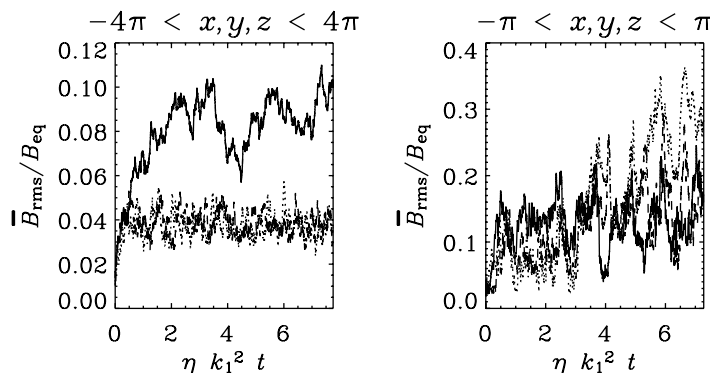


Figure 7. Comparison of the evolution of the rms values of the mean magnetic field obtained by averaging over xy planes (solid lines), yz planes (dotted lines), and xz planes (dashed lines) for domains of different size. Only in the case of a bigger domain, $-4\pi < x, y, z < 4\pi$, is there a weak mean field (solid curve). In the case of the smaller domain, $-\pi < x, y, z < \pi$, there is in principle also a mean field, but it is noisy and there is no preferred plane of averaging. In both cases $\nu = \eta = 2 \times 10^{-4}$.

are denoted by solid lines. Only in the case of the larger domain a mean field can be identified. In all other cases the resulting averages are dominated by ‘noise’. Nevertheless, even in the case of the bigger domain the amplitude of the mean field is small compared with the equipartition field strength, $B_{\text{eq}} = \langle \mu_0 \rho \mathbf{u}^2 \rangle^{1/2}$.

5. Inverse transfer from a localized source

Given that the problem of not seeing a large-scale field with a prolonged saturation phase of $\langle \overline{\mathbf{B}^2} \rangle$ is related to the lack of scale separation, we now devise a special experiment that can probably also easily be realized in the laboratory. The main idea is that the inverse transfer from small to large scales is primarily connected with the conservation of magnetic helicity (Frisch *et al* 1975), so it is a magnetic phenomenon that is best demonstrated using magnetic forcing in the induction equation. This was done in the seminal paper by Pouquet *et al* (1976) and the resistively slow build-up of magnetic energy has also been studied by Brandenburg *et al* (2002; see their figure 12).

The forcing needs to be helical in order to produce magnetic helicity. In order to have scale separation we apply the forcing only in small localized parts of the domain. Here we restrict ourselves to only a *single* localized source that has been modelled as

$$\mathcal{E}_{\text{ext}}(\mathbf{x}) = \sigma \nabla \times (\varphi \hat{\mathbf{z}}) + \nabla \times \nabla \times (\varphi \hat{\mathbf{z}}), \quad (8)$$

where we have chosen a Gaussian profile for φ with

$$\varphi(\mathbf{x}) = e_0 \exp(-\mathbf{x}^2/R^2), \quad (9)$$

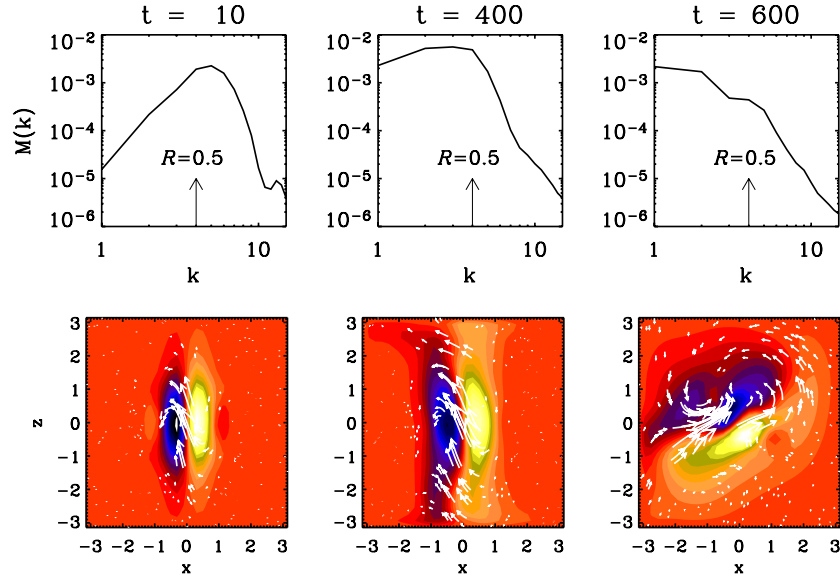


Figure 8. Evolution of magnetic energy spectra and slices of the magnetic field, driven by a localized helical electromotive force at the centre with $\sigma = 1$ and $e_0 = 0.02$. The vertical arrows indicate the effective forcing wavenumber, as obtained from equation (11). Here, $\nu = \eta = 5 \times 10^{-3}$, and so the three times shown in the figure correspond to $\eta k_1^2 t = 0.05, 2$ and 3 .

and $\sigma = 1$ is chosen for a helical flow. This yields

$$\mathcal{E}_{\text{ext}}(\mathbf{x}) = \begin{pmatrix} -2\sigma y/R^2 + 4xz/R^4 \\ 2\sigma x/R^2 + 4yz/R^4 \\ 4(R^2 - x^2 - y^2)/R^4 \end{pmatrix} \exp(-r^2/R^2). \quad (10)$$

Localized forcing functions of this form yield a peak in the spectrum at

$$k_{\text{peak}} = 2/R; \quad (11)$$

see also Mee and Brandenburg (2006), where a potential momentum forcing proportional to $\nabla\varphi$ was adopted. For all cases presented here we have chosen $R = 0.5$, so $k_{\text{peak}} = 4$. The forcing amplitude is varied between $e_0 = 0.005$ and 0.02 such that the maximum flow and Alfvén speeds remain subsonic.

Looking at figure 8 we see that a magnetic eddy is produced that begins to swell up until it loses its original up-down orientation and tilts sideways in a somewhat irregular manner. At the same time the overall magnetic energy has decreased somewhat, but most of the spectral energy is now at large scales. This type of behaviour is not seen without helicity injection, i.e. for $\sigma = 0$, as is demonstrated in figure 9.

6. Connection with the solar dynamo problem

We now wish to discuss the possible effects of magnetic helicity conservation that could be important for the solar dynamo. Obviously, only pieces of this question can be addressed at this point. Much of this has been discussed elsewhere (e.g. Blackman and Brandenburg (2002),

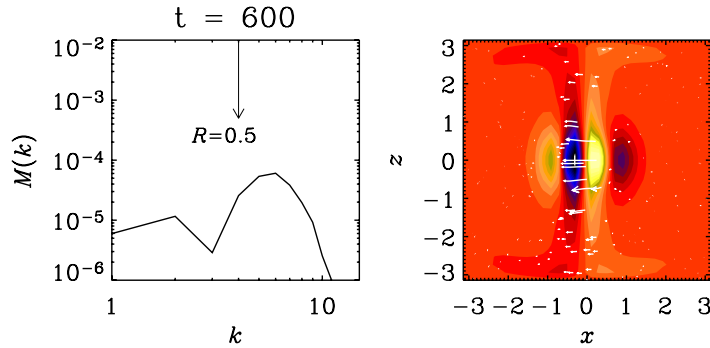


Figure 9. Magnetic energy spectrum and a slice of the magnetic field at $t = 600$ for the case of a nonhelical localized steady forcing at the centre with $\sigma = 0$ and $e_0 = 0.005$. Again, $\nu = \eta = 5 \times 10^{-3}$, and so the time shown in the figure corresponds to $\eta k_1^2 t = 3$.

(2003)) and is summarized in various reviews (e.g. Brandenburg and Subramanian (2005a), Brandenburg *et al* (2002)). One would generally expect magnetic helicity conservation to be important for affecting the cycle amplitude unless magnetic helicity is allowed to escape the dynamo domain.

Shear clearly plays an important role in dynamo processes. Two distinct effects can be identified. On the one hand shear can lead to so-called $\alpha\Omega$ dynamo action which is often oscillatory. On the other hand, shear can allow local magnetic and current helicity fluxes along lines of constant angular velocity (Subramanian and Brandenburg 2004, 2006; Vishniac and Cho 2001). We focus here on the former effect. In a closed domain magnetic helicity conservation acts as to produce a ‘counterproductive’ α effect that can saturate the dynamo, but it would not change the cycle frequency unless the turbulent magnetic diffusivity was also catastrophically affected. There has so far not been any clear evidence for catastrophic η_t quenching. Thus, we are at present not able to come to a conclusive result, which is mainly a consequence of the limited computing resources available. However, it is also clear that in all cases the magnetic field is in strong excess of the kinetic energy, and so any quenching would be dominated by classical (noncatastrophic) effects.

6.1. Catastrophic η_t quenching?

For a saturated $\alpha\Omega$ dynamo the cycle frequency is equal to $\omega_{\text{cyc}} = \eta_T k_1^2$ (Blackman and Brandenburg 2002), where $\eta_T = \eta_t + \eta$ is the total (turbulent plus microscopic) magnetically quenched diffusivity and k_1 is the largest wavenumber of the domain. This property is the key to what is perhaps the most robust method for determining the possible dependence of η_t on the magnetic field.

This was already attempted in Brandenburg *et al* (2002) using simulations with a sinusoidal shear profile, i.e. $\bar{U}_y = U_0 \sin k_1 x$. However, the result was not completely conclusive, because the solutions developed some additional complexity which resulted partly from the fact that shear strength and sign changed with x . In order to avoid this problem we consider now a linear shear profile of the form

$$\bar{U} = (0, Sx, 0)^T, \quad (12)$$

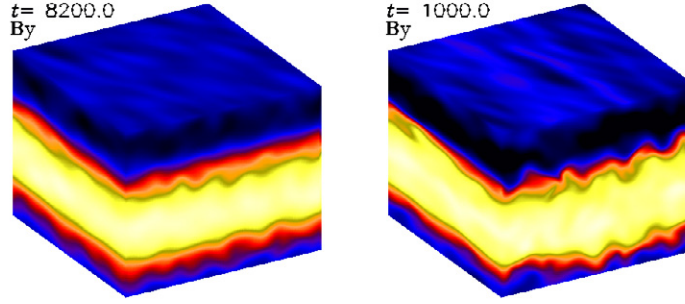


Figure 10. Visualization of the toroidal field B_y on the periphery of the shearing box in the presence of forced turbulence for shear strengths $S = -0.2$, $\nu = 5 \times 10^{-3}$, and two different values of η , 5×10^{-3} on the left and 5×10^{-4} on the right.

where S is the shear rate. We solve the governing equations using a shearing box approach with shearing-periodic boundary conditions; see Hawley *et al* (1995) and Brandenburg *et al* (1995).

The result of such simulations is shown in figure 10 for $S = -0.2$, $\nu = 5 \times 10^{-3}$, and $\eta = 2 \times 10^{-3}$ at a resolution of 64^3 (on the left) and $\eta = 5 \times 10^{-4}$ at a resolution of 256^3 (on the right). In both cases the field is cyclic corresponding to an upward travelling wave, and the times are chosen such that the magnetic field is in approximately the same phase in both figures. The fact that the dynamo wave travels in the positive z -direction is well understood as a consequence of a negative effective α (due to positive kinetic helicity in the forcing) and negative shear. The travelling wave behaviour is best seen in a space-time diagram shown in figure 11 for the simulation with $\eta = 2 \times 10^{-3}$. It turns out that $\omega_{\text{cyc}} = 0.0032$, and since $k_1 = 1$ this means $\eta_T = 0.0032$ and hence $\eta_t = 0.0012$ or $\eta_t/\eta = 0.6$. This is still quite small, but we will be continuing to run models at larger resolution to increase the value of η_t/η . In table 2, we have summarized these parameters also for a few other runs.

6.2. Catastrophic α quenching and nonlocality

The basic mechanism of catastrophic α quenching is now reasonably well understood. The basic recipe is this: whatever the mean turbulent electromotive force $\overline{\mathcal{E}}$ is, it leads not only to the production of large-scale magnetic fields via the standard mean field equation,

$$\frac{\partial \overline{\mathbf{B}}}{\partial t} = \nabla \times (\overline{\mathbf{U}} \times \overline{\mathbf{B}} + \overline{\mathcal{E}} - \eta \mu_0 \overline{\mathbf{J}}), \quad (13)$$

but it also leads to the production of a magnetic α effect, α_M , which characterizes the production of internal twist in the system. Its governing equation is

$$\frac{\partial \alpha_M}{\partial t} + \nabla \cdot \overline{\mathcal{F}} = -2\eta_t k_f^2 \left(\frac{\overline{\mathcal{E}} \cdot \overline{\mathbf{B}}}{B_{\text{eq}}^2} + \frac{\alpha_M}{R_m} \right). \quad (14)$$

Here we have allowed for the possibility of an additional flux of small-scale magnetic helicity. Also, in this equation R_m is meant to represent η_t/η by definition; see Blackman and

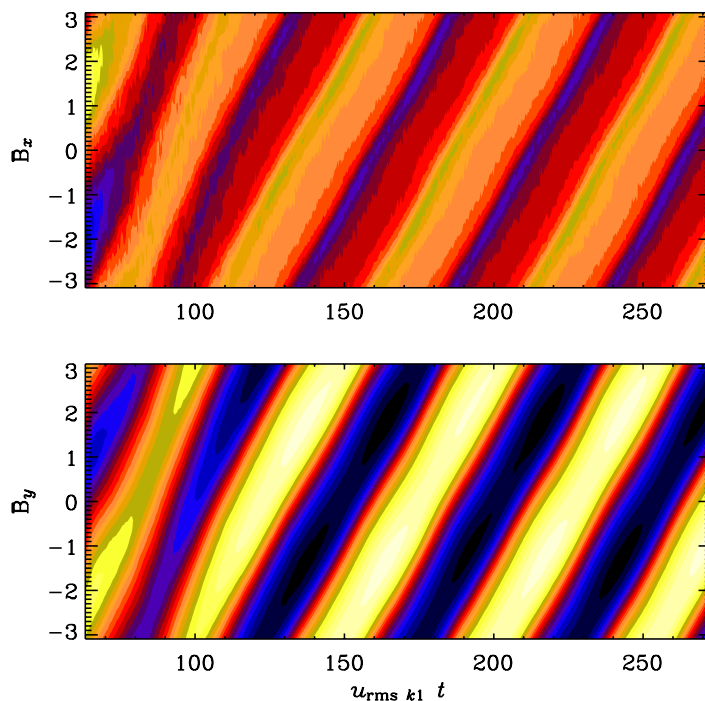


Figure 11. Space-time, butterfly, or simply zt diagram of $\overline{B}_x(z, t)$ and $\overline{B}_y(z, t)$ for forced turbulence with shear, with $S = -0.2$, $\nu = 5 \times 10^{-3}$ and $\eta = 5 \times 10^{-3}$.

Table 2. Summary of runs with uniform shear and different values of the magnetic diffusivity and either constant kinematic viscosity or constant magnetic Prandtl number.

ν	η	ω_{cyc}	η_t	η_t/η	$ \overline{\mathbf{B}} /B_{\text{eq}}$
5×10^{-3}	2×10^{-3}	3.2×10^{-3}	1.2×10^{-3}	0.6	10
5×10^{-3}	1×10^{-3}	2.0×10^{-3}	1.0×10^{-3}	1.0	13
5×10^{-3}	5×10^{-4}	1.2×10^{-3}	0.7×10^{-3}	1.4	16
5×10^{-3}	2×10^{-4}	0.7×10^{-3}	0.5×10^{-3}	2.5	18
5×10^{-3}	5×10^{-3}	5.2×10^{-3}	0.2×10^{-3}	0.04	7.6
2×10^{-3}	2×10^{-3}	3.0×10^{-3}	1.0×10^{-3}	0.5	14

Brandenburg (2002) for details. Note that the magnetic helicity equation is unaffected by the large-scale velocity term, $\overline{\mathbf{U}} \times \overline{\mathbf{B}}$.

It is important to realize that the possibility of catastrophic quenching is quite general and not restricted to the local α effect formula considered here. In some recent solar dynamo models the so-called Babcock–Leighton mechanism is used (e.g. Dikpati and Charbonneau (1999)). Here one assumes that there is some source term to the electromotive force that is localized near the surface, but it is proportional to the toroidal field at the bottom of the convection zone. This effect is sometimes thought of being distinct from the usual α effect in that it allows for the generation of super-equipartition field strengths.

Formally, the Babcock–Leighton mechanism is just a nonlocal α effect where the multiplication in $\alpha \overline{\mathbf{B}}$ is replaced by a convolution, $\hat{\alpha} \circ \overline{\mathbf{B}}$, where $\hat{\alpha}$ is an integral kernel. Applying

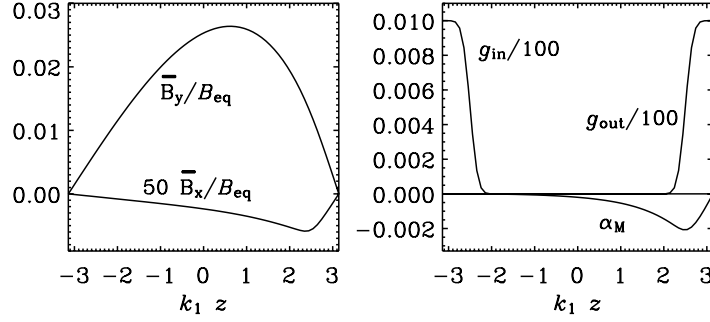


Figure 12. Profiles of the magnetic field and the magnetic contribution to the α effect for the non-local dynamo model with $R_m = 10^3$.

the same idea also to the turbulent magnetic diffusivity $\hat{\eta}_t(z, z')$, leads to an expression for $\bar{\mathcal{E}}(z, t)$ of the form

$$\bar{\mathcal{E}}(z, t) = \int_{z_1}^{z_2} \hat{\alpha}(z, z') \bar{\mathbf{B}}(z', t) dz' - \int_{z_1}^{z_2} \hat{\eta}(z, z') \bar{\mathbf{J}}(z', t) dz'. \quad (15)$$

The possibility of nonlocal α and η effects has been inferred also from simulation data of magneto-rotational turbulence in accretion discs (Brandenburg and Sokoloff 2002). Non-local α effects are conveniently characterized in terms of its spectral decomposition,

$$\tilde{\alpha}(k) = \int_{z_1}^{z_2} \sin kz \sin kz' \hat{\alpha}(z, z') dz dz'. \quad (16)$$

This technique is particularly convenient because in Fourier space the convolution corresponds to a multiplication.

In the following we restrict ourselves to a simple expression of the form

$$\hat{\alpha}(z, z') = \alpha_0 g_{out}(z) g_{in}(z'), \quad (17)$$

where

$$g_{out}(z) = \frac{1}{2} \left[1 + \operatorname{erf} \left(\frac{z - z_2}{d} \right) \right], \quad (18)$$

$$g_{in}(z') = \frac{1}{2} \left[1 - \operatorname{erf} \left(\frac{z' - z_1}{d} \right) \right] \quad (19)$$

are simple profile functions representing the peak of the source function near $z = z_2$ with a sensitivity for fields located near $z = z_1$. For the following we choose $-z_1 = z_2 = 2.5$ and $d = 0.05$ in the domain $-\pi < z < \pi$; see the right-hand panel of figure 12. The resulting profile of $\tilde{\alpha}(k)$ according to equation (16) is shown in figure 13.

We solve equations (13) and (14) numerically for the case $\bar{\mathcal{F}} = 0$ using an implicit scheme for α_M by writing the equation in the form

$$\frac{\alpha_M^{n+1} - \alpha_M^n}{\delta t} + 2\eta_t k_f^2 \frac{\bar{\mathcal{E}}_0 \cdot \bar{\mathbf{B}}}{B_{eq}^2} + \eta k_f^2 \left(1 + R_m \frac{\bar{\mathbf{B}}^2}{B_{eq}^2} \right) (\alpha_M^{n+1} + \alpha_M^n) = 0, \quad (20)$$

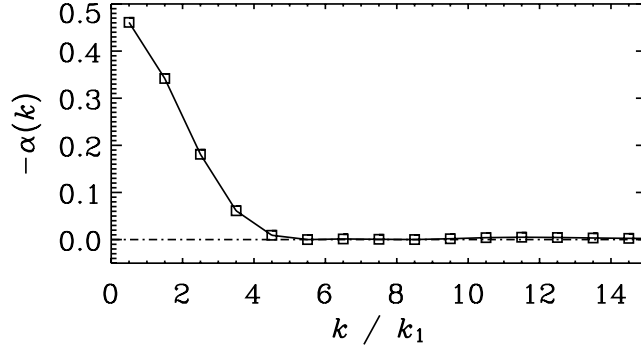


Figure 13. Profile of the α kernel for the non-local (Babcock–Leighton type) dynamo model computed using equation (16).

where $\bar{\mathcal{E}}_0 = \bar{\mathcal{E}} - \alpha_M \bar{\mathbf{B}}$ is the electromotive force without the magnetic quenching term. Equation (20) is then solved for α_M^{n+1} at the new time, $t_{n+1} = t_n + \delta t$, using for $\bar{\mathbf{B}}$ the value at the present time level t_n , i.e.

$$\alpha_M^{n+1} = (1 + Q)^{-1} \left[(1 - Q)\alpha_M^n - 2\eta_t k_f^2 \delta t \frac{\bar{\mathcal{E}}_0 \cdot \bar{\mathbf{B}}}{B_{\text{eq}}^2} \right], \quad (21)$$

where $Q = \eta k_f^2 \delta t (1 + R_m \bar{\mathbf{B}}^2 / B_{\text{eq}}^2)$. We have considered a model using linear shear of the form (12). The strength of shear and α effect are quantified by the nondimensional numbers

$$C_S = \frac{S}{\eta_t k_1^2}, \quad C_\alpha = \frac{\alpha}{\eta_t k_1}, \quad (22)$$

where $k_1 = 1$ is the smallest wavenumber in the computational domain. In the following we use $C_S = 100$, $C_\alpha = 0.1$, and $k_f/k_1 = 5$. In many cases an explicit treatment of the α_M equation suffices (e.g. Blackman and Brandenburg (2002)), but in the present case an explicit solution algorithm was found to be unstable.

It turns out that most of the field is generated in the middle of the domain, while most of the quenching via α_M occurs near the top layers around $z = z_2$; see figure 12. Nevertheless, as expected, this model still experiences catastrophic quenching; see figure 14. These results look quite similar to those obtained for local α profiles (Brandenburg and Subramanian 2005b). We note that for $R_m = 10^4$ it is important to perform the calculations using double precision arithmetics.

6.3. Location of the dynamo

The location of the solar dynamo is rather uncertain. Particularly unclear is the location where most of the toroidal field resides. The standard thinking since the 1980s is that most of the toroidal field can only reside at the base of the convection zone, because magnetic buoyancy would remove the field on a short timescale. However, it turned out that downward pumping of magnetic field helps to keep the magnetic field inside the convection zone. On the other hand, the toroidal field has been argued to be actually quite strong, such that it would exceed the

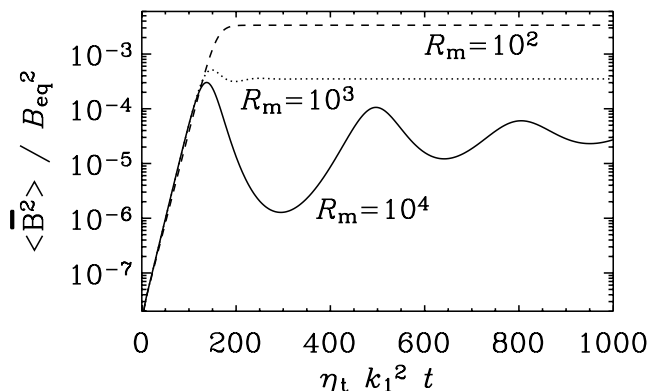


Figure 14. Evolution of the magnetic energy of the large-scale field for R_m between 10^2 and 10^4 for the non-local dynamo model. For large values of R_m the linear growth rate reaches an asymptotic value, but the nonlinear saturation amplitude continues to depend on R_m .

equipartition field strength by factors as large as 100. Furthermore, stability of such strong fields even beneath the convection zone have recently been put under doubt (Arlt *et al* 2007, Kitchatinov and Rüdiger 2007). Whether or not such strong fields could be generated by a turbulent dynamo is unclear. This led to the proposal that the solar dynamo may instead be located in the bulk of the convection zone and that the mean fields are at most comparable in strength to the equipartition field strength (Brandenburg 2005).

Astrophysical dynamos are not expected to be catastrophically quenched, because they are likely to shed excess small-scale magnetic helicity through magnetic helicity fluxes. This would mean that the quenching through α_M is much weaker than the other nonlinearities, e.g. suppression of the mean flow or of α_K itself. The latter can be *approximated* by the more conventional expression $\alpha_K = \alpha_{K0}/(1 + \mathbf{B}^2/B_{eq}^2)$ (for detailed expressions see Rogachevskii and Kleeorin (2000)).

If the solar dynamo does indeed work in a distributed fashion, then the meridional circulation is probably no longer important for determining the cycle period and the equatorward migration of the magnetic flux belts. Instead, the dynamo may be essentially of a standard $\alpha\Omega$ type. However, an important problem arises from the fact that the near-surface shear layer, where $\partial\Omega/\partial r < 0$, is rather thin. Given that the aspect ratio of magnetic flux belts is usually of order unity, it is difficult to envisage how one can explain the rather broad latitudinal distribution of flux of the same sign.

As a possible solution to this problem one might think of the effects of magnetic helicity transport and possibly the anisotropy of the turbulent magnetic diffusivity. However, magnetic helicity fluxes modify primarily the effective α and it is not clear that they affect the aspect ratio of the toroidal flux belts. In the following we address the effect of an anisotropic magnetic diffusivity. Based on the dispersion relation for a dynamo wave in a two-dimensional domain (see, e.g. Brandenburg and Subramanian (2005a), section 6.5.2),

$$\lambda = -\eta_T(k_x^2 + \epsilon k_z^2) + \sqrt{\frac{1}{2}\alpha S k_x}, \quad (23)$$

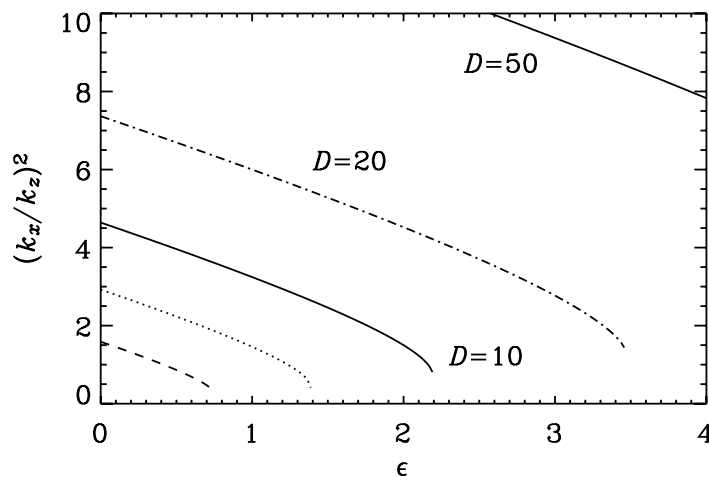


Figure 15. Aspect ratio as a function of the degree of anisotropy, ϵ for $D = 2$ (dashed line), 5 (dotted line), 10, 20 and 50. When the lines stop for small values of $\kappa = k_x/k_z$ there are no solutions any more.

where ϵ is the degree of anisotropy, we find that in the marginally excited case, $\lambda = 0$, the value of k_x can be obtained iteratively. For this purpose, let us define the aspect ratio as $\kappa = k_x/k_z$, which is then given by

$$\kappa^2 + \epsilon = \sqrt{\frac{1}{2}\alpha S\kappa/\eta_T^2 k_z^3}. \quad (24)$$

We define the dynamo number as

$$D = \frac{1}{2}\alpha S/\eta_T^2 k_z^3, \quad (25)$$

so equation (24) reduces to

$$\kappa^2 = \sqrt{D\kappa} - \epsilon, \quad (26)$$

which can be solved iteratively. The result is shown in figure 15. In the special case $\epsilon = 0$ we have $\kappa = D^{1/3}$.

It turns out that anisotropic diffusion tends to increase the ratio $\kappa = k_x/k_z$, so the wavelength in the latitudinal (or x -)direction becomes smaller, making the problem even worse. Obviously one must be careful with linear theory, so this result may not be too meaningful, but in the absence of any other evidence there is currently no particular reason to expect anisotropic diffusion being a solution to the problem of the aspect ratio.

6.4. Predictability in distributed dynamos

Flux transport dynamos have been used for predicting the strength of the next solar cycle, Cycle 24 (see Clarke (2006) for a general assessment). The outcome depends essentially on the way the observed solar activity is used to keep the evolution of the model in sync with the Sun. In Dikpati and Gilman (2006, 2006) the sunspot number is used as a proxy of the poloidal field production by a source term near the surface. On the other hand, in Choudhuri *et al* (2007) the

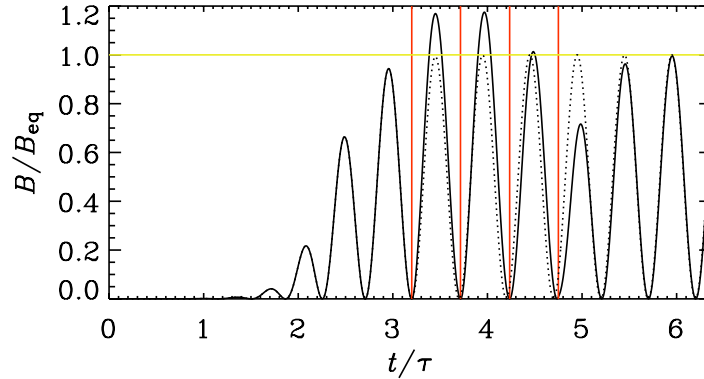


Figure 16. Simple dynamo model with dynamo number $D = 4$ with initial condition $A = 0.01$ and $B = 0$. The model reaches saturation at $t/\tau \approx 3$. The poloidal field is rescaled by factors 1.25, 1.23, 1.00 and 0.60 during the minima marked by vertical lines. The unscaled model is overplotted as a dotted line. Note the weak cycle amplitude at $t/\tau \approx 5$, corresponding to Cycle 24.

observed poloidal field around the poles is used to correct the poloidal field in the upper part of their model during solar minimum. Regardless of the fact that the outcomes can be very different (strong Cycle 24 in the former model and weak Cycle 24 in the latter), it is clear that this topic has attracted significant attention (Clarke 2006, Cameron and Schüssler 2007, Tobias *et al* 2006) and has led to the impression that the solar dynamo problem might be solved.

The point of this section is to show that the predictive power of a model is not very sensitive to the details, and that even in the extreme case of a fully distributed toy model similar predictability can be achieved. To demonstrate this, we consider here the following simple model equations that are obtained from a single mode truncation of a one-dimensional periodic model, i.e.

$$\frac{dA}{dt} = \alpha B - \tau^{-1} A, \quad (27)$$

$$\frac{dB}{dt} = ik\Omega' A - \tau^{-1} B, \quad (28)$$

for the complex variables A and B , that characterize the poloidal and toroidal fields, respectively (Durney and Robinson 1982). Here, $\tau = (\eta_t k^2)^{-1}$ is the turbulent magnetic diffusion time, Ω' is the radial gradient of the angular velocity, and α is the α effect. We assume here a simple form of α quenching with $\alpha = \alpha_0 / (1 + |B|^2 / B_{\text{eq}}^2)$, where α_0 is the kinematic value of the α effect, and B_{eq} is the equipartition field strength. The nondimensional dynamo number, $D = \alpha_0 \Omega' k L \tau^{-2}$ has to exceed the value $D = 2$ for dynamo action.

Following Choudhuri *et al* (2007) we use normalized values of the observed dipole moment (as given by Svalgaard *et al* (2005)) to correct the poloidal field amplitude A by factors 1.25, 1.23, 1.00 and 0.60 after Cycles 20, 21, 22 and 23, respectively. The result is shown in figure 16. The maxima in $|B|$ after each of the four rescalings are 1.17, 1.17, 1.02 and 0.71 times the usual values. Applied to the Sun, this means that the next cycle will indeed be about 30% weaker than the previous one. This is obviously in perfect agreement with the model of Choudhuri *et al* (2007) and of course the earlier investigations by Svalgaard *et al* (2005).

7. Conclusions

There has been tremendous progress in dynamo theory since the beginning of the millennium, both theoretically and experimentally. In this paper we do not intend to review any of this progress. Instead, we have focused on a number of new ideas that emerged in an attempt to connect theory and experiments. The relevance of experiments is not immediately obvious because in experiments the value of R_m is currently below 50 or so, while simulations can reach values in the order of 1000. On the other hand, in experiments the magnetic Prandtl number is small (10^{-5}), which is quite similar to the value in the Sun and other stars. To reach interesting values of R_m that allow for dynamo action or other effects to occur, the fluid Reynolds number has to be very large (in excess of 10^6 or so), which is out of reach of simulations even in the intermediate future.

On the other hand, experiments are now beginning to produce dynamo action in unconstrained flows (Monchaux *et al* 2007), and corresponding experiments are now beginning to produce results that can meaningfully be compared with experiments. Examples include the work of Nore *et al* (1997) for simulating flows close to those in the VKS experiment, and approximations to the VKS flow in terms of TG flows (Mininni *et al* 2005b, Ponty *et al* 2004). Although neither of these cases is anywhere near the conditions relevant to the Sun, it is conceivable that the theoretical investigations that have been undertaken in just the last few years (e.g. regarding magnetic helicity conservation and helicity fluxes) can lead to new paradigms that can in principle be tested experimentally (e.g. the phenomenon of inverse cascade-type behaviour).

Even though progress is rapid, and success appears sometimes in reach, there are still a number of problems that are poorly understood. An example concerns the magnetic helicity flux whose effects are manifested in coronal mass ejections (Démoulin *et al* 2002), but they have hardly been incorporated in dynamo models with the aim to alleviate the otherwise catastrophic quenching.

Acknowledgments

We thank Eric Blackman for making useful suggestions to an earlier version of the paper. We acknowledge the allocation of computing resources provided by the Centers for Scientific Computing in Denmark (DCSC), Finland (CSC), and Sweden (PDC).

Appendix A. Magnetic versus kinetic helicity conservation

In this appendix, we want to show why there is such a dramatic difference between the conservation of magnetic and kinetic helicities. The kinetic helicity is indeed conserved if there is no magnetic field, i.e. no Lorentz force, and if $\nu = 0$ exactly. Let us also assume $\nabla \cdot \mathbf{A} = \nabla \cdot \mathbf{U} = 0$ for simplicity, although this is not critical. The pair of analogous equations can then be written as

$$\frac{\partial \mathbf{A}}{\partial t} = \mathbf{U} \times \mathbf{B} - \eta \mathbf{J} - \nabla \phi + \mathcal{E}_{\text{ext}}, \quad (\text{A.1})$$

$$\frac{\partial \mathbf{U}}{\partial t} = \mathbf{U} \times \mathbf{W} - \nu \mathbf{Q} - \nabla p + \mathcal{F}_{\text{ext}}. \quad (\text{A.2})$$

For later reference we also quote here the curled evolution equations, where $\mathbf{B} = \nabla \times \mathbf{A}$ is the magnetic field and $\mathbf{W} = \nabla \times \mathbf{U}$ is the vorticity, i.e.

$$\frac{\partial \mathbf{B}}{\partial t} = \nabla \times (\mathbf{U} \times \mathbf{B}) - \eta \nabla \times \mathbf{J} + \nabla \times \mathcal{E}_{\text{ext}}, \quad (\text{A.3})$$

$$\frac{\partial \mathbf{W}}{\partial t} = \nabla \times (\mathbf{U} \times \mathbf{W}) - \nu \nabla \times \mathbf{Q} + \nabla \times \mathcal{F}_{\text{ext}}. \quad (\text{A.4})$$

Note that $\nabla \cdot \mathbf{B} = \nabla \cdot \mathbf{W} = 0$ is automatically fulfilled. Denoting, as usual, volume averages by angular brackets, and assuming periodic boundaries, the evolution equations for the two helicities are

$$\frac{\partial}{\partial t} \langle \mathbf{A} \cdot \mathbf{B} \rangle = -2\eta \langle \mathbf{J} \cdot \mathbf{B} \rangle + 2 \langle \mathbf{B} \cdot \mathcal{E}_{\text{ext}} \rangle, \quad (\text{A.5})$$

$$\frac{\partial}{\partial t} \langle \mathbf{U} \cdot \mathbf{W} \rangle = -2\nu \langle \mathbf{Q} \cdot \mathbf{W} \rangle + 2 \langle \mathbf{W} \cdot \mathcal{F}_{\text{ext}} \rangle. \quad (\text{A.6})$$

For completeness we also give here the evolution equations for the energy norms,

$$\frac{\partial}{\partial t} \frac{1}{2} \langle \mathbf{A}^2 \rangle = -\langle \mathbf{U} \cdot (\mathbf{A} \times \mathbf{B}) \rangle - \eta \langle \mathbf{B}^2 \rangle + \langle \mathbf{A} \cdot \mathcal{E}_{\text{ext}} \rangle, \quad (\text{A.7})$$

$$\frac{\partial}{\partial t} \frac{1}{2} \langle \mathbf{U}^2 \rangle = -\langle \mathbf{U} \cdot (\mathbf{U} \times \mathbf{W}) \rangle - \nu \langle \mathbf{W}^2 \rangle + \langle \mathbf{U} \cdot \mathcal{F}_{\text{ext}} \rangle, \quad (\text{A.8})$$

$$\frac{\partial}{\partial t} \frac{1}{2} \langle \mathbf{B}^2 \rangle = -\langle \mathbf{U} \cdot (\mathbf{J} \times \mathbf{B}) \rangle - \eta \langle \mathbf{J}^2 \rangle + \langle \mathbf{J} \cdot \mathcal{E}_{\text{ext}} \rangle, \quad (\text{A.9})$$

$$\frac{\partial}{\partial t} \frac{1}{2} \langle \mathbf{W}^2 \rangle = -\langle \mathbf{U} \cdot (\mathbf{Q} \times \mathbf{W}) \rangle - \nu \langle \mathbf{Q}^2 \rangle + \langle \mathbf{Q} \cdot \mathcal{F}_{\text{ext}} \rangle. \quad (\text{A.10})$$

Note that we kept the term $\langle \mathbf{U} \cdot (\mathbf{U} \times \mathbf{W}) \rangle = 0$ in order to enhance the formal analogy of the equations. In the helicity equations one could restore two similarly redundant terms,

$$\frac{1}{2} \frac{\partial}{\partial t} \langle \mathbf{A} \cdot \mathbf{B} \rangle = -\langle \mathbf{U} \cdot (\mathbf{B} \times \mathbf{B}) \rangle - \eta \langle \mathbf{J} \cdot \mathbf{B} \rangle + \langle \mathbf{B} \cdot \mathcal{E}_{\text{ext}} \rangle, \quad (\text{A.11})$$

$$\frac{1}{2} \frac{\partial}{\partial t} \langle \mathbf{U} \cdot \mathbf{W} \rangle = -\langle \mathbf{U} \cdot (\mathbf{W} \times \mathbf{W}) \rangle - \nu \langle \mathbf{Q} \cdot \mathbf{W} \rangle + \langle \mathbf{W} \cdot \mathcal{F}_{\text{ext}} \rangle. \quad (\text{A.12})$$

In conclusion, all the evolution equations have the following three terms: an internal driving term such as $\langle \mathbf{U} \cdot (\mathbf{J} \times \mathbf{B}) \rangle$, an external driving term such as $\langle \mathbf{U} \cdot \mathcal{F}_{\text{ext}} \rangle$, and a viscous or resistive loss term. In the magnetic energy equation there is the internal driving term (work done against the Lorentz force), but usually no external driving term, since $\mathcal{E}_{\text{ext}} = 0$ is assumed here. The kinetic energy equation, on the other hand, does not have an internal driving term, because

$\langle \mathbf{U} \cdot (\mathbf{U} \times \mathbf{W}) \rangle = 0$. Thus, both kinetic and magnetic energy equations have driving terms, so we have

$$\frac{\partial}{\partial t} \frac{1}{2} \langle \mathbf{B}^2 \rangle = -\langle \mathbf{U} \cdot (\mathbf{J} \times \mathbf{B}) \rangle - \eta \langle \mathbf{J}^2 \rangle, \quad (\text{A.13})$$

$$\frac{\partial}{\partial t} \frac{1}{2} \langle \mathbf{U}^2 \rangle = \langle \mathbf{U} \cdot \mathcal{F}_{\text{ext}} \rangle - \nu \langle \mathbf{W}^2 \rangle. \quad (\text{A.14})$$

Thus, in a statistically steady state, the dissipative terms have to balance the corresponding driving terms. In the limit of large magnetic and fluid Reynolds numbers this leads to the asymptotic scalings

$$|\mathbf{J}| \sim \eta^{-1/2}, \quad |\mathbf{W}| \sim \nu^{-1/2}. \quad (\text{A.15})$$

At the same time, because kinetic and magnetic energies are bounded, magnetic field strength and velocity do not diverge but stay independent of η and ν , respectively. This also implies that the typical inverse length scales scale like

$$k \sim |\mathbf{W}|/|\mathbf{U}| \sim \nu^{-1/2}, \quad (\text{A.16})$$

and hence that

$$|\mathbf{Q}| \sim k|\mathbf{W}| \sim \nu^{-1}, \quad (\text{A.17})$$

so that the magnetic and kinetic helicity dissipation terms scale like

$$|\eta \langle \mathbf{J} \cdot \mathbf{B} \rangle| \rightarrow \eta^{1/2} \rightarrow 0, \quad (\text{A.18})$$

$$|\nu \langle \mathbf{Q} \cdot \mathbf{W} \rangle| \rightarrow \nu^{-1/2} \rightarrow \infty, \quad (\text{A.19})$$

which highlights the fundamental difference between kinetic and magnetic helicity conservation when η and ν are not zero but small.

Appendix B. The forcing function

For completeness we specify here the forcing function used in the present paper.⁶ It is defined as

$$\mathbf{f}(\mathbf{x}, t) = \text{Re}\{N \mathbf{f}_{k(t)} \exp[i\mathbf{k}(t) \cdot \mathbf{x} + i\phi(t)]\}, \quad (\text{B.1})$$

where \mathbf{x} is the position vector. The wavevector $\mathbf{k}(t)$ and the random phase $-\pi < \phi(t) \leq \pi$ change at every time step, so $\mathbf{f}(\mathbf{x}, t)$ is δ -correlated in time. For the time-integrated forcing function to be independent of the length of the time step δt , the normalization factor N has to be proportional to $\delta t^{-1/2}$. On dimensional grounds it is chosen to be $N = f_0 c_s (|\mathbf{k}| c_s / \delta t)^{1/2}$,

⁶ This forcing function was also used by Brandenburg (2001), but in his equation (5) the factor 2 in the denominator should have been replaced by $\sqrt{2}$ for a proper normalization.

where f_0 is a nondimensional forcing amplitude. At each time step we randomly select one of many possible wavevectors in a certain range around a given forcing wavenumber. The average wavenumber is referred to as k_f . We force the system with transverse helical waves,

$$\mathbf{f}_k = \mathbf{R} \cdot \mathbf{f}_k^{(\text{nohel})} \quad \text{with} \quad R_{ij} = \frac{\delta_{ij} - i\sigma\epsilon_{ijk}\hat{k}_k}{\sqrt{1 + \sigma^2}}, \quad (\text{B.2})$$

where $\sigma = 1$ for positive helicity of the forcing function,

$$\mathbf{f}_k^{(\text{nohel})} = (\mathbf{k} \times \hat{\mathbf{e}}) / \sqrt{k^2 - (\mathbf{k} \cdot \hat{\mathbf{e}})^2}, \quad (\text{B.3})$$

is a nonhelical forcing function, and $\hat{\mathbf{e}}$ is an arbitrary unit vector not aligned with \mathbf{k} ; note that $|\mathbf{f}_k|^2 = 1$.

Appendix C. One-mode truncation of the Blackman–Field model

A one-mode truncation of the dynamically quenched α effect has been studied by Blackman and Brandenburg (2002), where $\bar{\mathbf{B}}(z, t) = \hat{\mathbf{B}}(t) \exp(ik_1 z)$ has been assumed. Here we include the explicit time dependence of the electromotive force $\bar{\mathcal{E}}(z, t) = \hat{\mathcal{E}}(t) \exp(ik_1 z)$, so our model equations are

$$\frac{d\hat{\mathbf{B}}}{dt} = i\mathbf{k}_1 \times (\hat{\mathcal{E}} - \eta\hat{\mathbf{J}}), \quad (\text{C.1})$$

$$\frac{d\hat{\mathcal{E}}}{dt} = \tilde{\alpha}\hat{\mathbf{B}} - \tilde{\eta}_t\hat{\mathbf{J}} - \frac{\hat{\mathcal{E}}}{\tau}, \quad (\text{C.2})$$

$$\frac{d\alpha_M}{dt} = -2\eta_t k_f^2 \left[\frac{\text{Re}(\hat{\mathcal{E}}^* \cdot \hat{\mathbf{B}})}{B_{\text{eq}}^2} + \frac{\alpha_M}{R_m} \right], \quad (\text{C.3})$$

where $\hat{\mathbf{B}}$ and $\hat{\mathcal{E}}$ are complex and α_M a real dependent variable, $\mathbf{k}_1 = (0, 0, k_1)^T$ is the wavevector, $\alpha = \alpha_K + \alpha_M$ with $\alpha = \tau\tilde{\alpha}$ and $\eta_t = \tau\tilde{\eta}_t$, and τ is the relaxation time. The closure assumption consists in representing the triple correlations by the damping term $\hat{\mathcal{E}}/\tau$.

In order to associate this model with a simulation, we use the values of k_f/k_1 , R_m and chose a value of St to determine the following set of model parameters: $u_{\text{rms}} = 3\eta_t k_f / \text{St}$, $\tau = \text{St} / (u_{\text{rms}} k_f)$, and $\alpha_K = \eta_t k_f$, which assumes perfectly helical turbulence, which is obviously not realistic for TG flow dynamos.

References

- Arlt R, Sule A and Rüdiger G 2007 *Astron. Astrophys.* **461** 295
 Blackman E G and Brandenburg A 2002 *Astrophys. J.* **579** 359
 Blackman E G and Brandenburg A 2003 *Astrophys. J.* **584** L99
 Blackman E G and Field G B 2002 *Phys. Rev. Lett.* **89** 265007

- Brachet M E 1991 *Fluid Dyn. Res.* **8** 1
- Brandenburg A 2001 *Astrophys. J.* **550** 824
- Brandenburg A 2005 *Astrophys. J.* **625** 539
- Brandenburg A and Sokoloff D 2002 *Geophys. Astrophys. Fluid Dyn.* **96** 319
- Brandenburg A and Subramanian K 2005 *Phys. Rep.* **417** 1
- Brandenburg A and Subramanian K 2005 *Astron. Nachr.* **326** 400
- Brandenburg A, Nordlund Å, Stein R F and Torkelsson U 1995 *Astrophys. J.* **446** 741
- Brandenburg A, Dobler W and Subramanian K 2002 *Astron. Nachr.* **323** 99
- Brandenburg A, Käpylä P and Mohammed A 2004 *Phys. Fluids* **16** 1020
- Cameron R and Schüssler M 2007 *Astrophys. J.* **659** 801
- Choudhuri A R, Chatterjee P and Jiang J 2007 *Phys. Rev. Lett.* **98** 131103
- Clarke S 2006 *Nature* **441** 402
- Démoulin P, Mandrini C H, van Driel-Gesztelyi L, Lopez Fuentes M C and Aulanier G 2002 *Sol. Phys.* **207** 87
- Dikpati M and Charbonneau P 1999 *Astrophys. J.* **518** 508
- Dikpati M and Gilman P A 2006 *Astrophys. J.* **649** 498
- Dikpati M, de Toma G and Gilman P A 2006 *Geophys. Res. Lett.* **33** L05102
- Durney B R and Robinson R D 1982 *Astrophys. J.* **253** 290
- Fauve S and Pétrélis F 2003 *Peyresq Lectures on Nonlinear Phenomena* vol 2, ed J-A Sepulchre (Singapore: World Scientific)
- Frisch U, Pouquet A, Léorat J and Mazure A 1975 *J. Fluid Mech.* **68** 769
- Hawley J F, Gammie C F and Balbus S A 1995 *Astrophys. J.* **440** 742
- Kenjereš S and Hanjalić K 2007 *Phys. Rev. Lett.* **98** 104501
- Kitchatinov L L and Rüdiger G 2007 *Astron. Astrophys.* submitted (*Preprint astro-ph/0701847*)
- Mee A J and Brandenburg A 2006 *Mon. Not. R. Astron. Soc.* **370** 415
- Mininni P D, Gómez D O, Mahajan S M 2005a *Astrophys. J.* **619** 1019
- Mininni P, Alexakis A, Pouquet A 2005b *Phys. Rev. E* **72** 046302
- Monchaux R *et al* 2007 *Phys. Rev. Lett.* **98** 044502
- Morin V 2005 *PhD thesis* Université Paris VII
- Nakano T 1985 *Prog. Theor. Phys.* **73** 629
- Nore C, Brachet M E, Politano H and Pouquet A 1997 *Phys. Plasmas* **4** 1
- Nore C, Martin Witkowski L, Foucault E, Pécheux J, Daube O and Le Quéré P 2006 *Phys. Fluids* **18** 54102
- Ponty Y, Politano H and Pinton J-F 2004 *Phys. Rev. Lett.* **92** 144503
- Ponty Y, Mininni P D, Montgomery D C, Pinton J-F, Politano H and Pouquet A 2005 *Phys. Rev. Lett.* **94** 164502
- Pouquet A, Frisch U and Léorat J 1976 *J. Fluid Mech.* **77** 321
- Rogachevskii I and Kleorin N 2000 *Phys. Rev. E* **61** 5202
- Subramanian K and Brandenburg A 2004 *Phys. Rev. Lett.* **93** 205001
- Subramanian K and Brandenburg A 2006 *Astrophys. J.* **648** L71
- Svalgaard L, Cliver E W and Kamide Y 2005 *Geophys. Res. Lett.* **32** L01104
- Tobias S, Hughes D and Weiss N 2006 *Nature* **442** 26
- Vishniac E T and Cho J 2001 *Astrophys. J.* **550** 752